

Advanced Characterisation of Pore Structure in Next-Generation Reactor Graphites

Bradley Moresby-White^a, Katie L. Jones^{a,*}, G. Peter Matthews^a, Giuliano M. Laudone^a

^a*Faculty of Science and Engineering, University of Plymouth, Plymouth, UK*

Abstract

Nuclear grade graphite

Keywords: keyword, keyword, keyword

1. Introduction

2. Methodology

2.1. Materials

Virgin graphite samples of two grades, IG-110 and IG-430, were supplied by Toyo Tanso LtdTM, Osaka, Japan. The properties of both grades are tabulated (Table 1). IG-110 is currently employed in the three existing HTGRs worldwide, while IG-430 is designed to deliver increased density, strength, and thermal conductivity for future applications.[1] (Table 1). Both grades comply with ASTMD7219-19, including the requirement for a minimum bulk density exceeding 1.7 g/cm³ [2] (Table 1).

Is this necessary?
I do like it, talking about the standards, but it is a bit of a tangent.

for the following table, better to directly cite the manuf?

2.2. Sample preparation

Cuboids were sub-sampled from the virgin graphite blocks, with dimensions of approximately 10mm x 10mm x 100mm. The sub-samples were further subsampled into cuboids of side lengths 7mm, providing 3 cuboids per grade. Samples were polished via SiC polishing pads up to a grit size of P5000, to minimise topographical variations induced by sample preparation that may cause artefacts during either SEM imaging or low pressure gas adsorption [4, 3]. Samples were sonicated in 2-propanol for 24h to remove any contaminants, including the lubricant used in the machining process or silica particles introduced during polishing.

Samples were then dried under vacuum for 12 h at 305±5 °C using the BELPREP-vac (MicrotracBEL, Japan) in order to remove any residual moisture introduced during the sonication process.

2.3. Scanning Electron Microscopy (SEM)

SEM microscopy fundamentally consists of an electron source, confined to a thin beam, accelerated towards the sample. The resulting electrons strike the photomultiplier, generating electrical signals that are subsequently amplified [5, 6]. For SEM analysis of the surface features of nuclear-grade graphite, the signal of interest is the secondary electrons, which are produced when the incident electrons from the beam excite electrons within the atoms of the graphite surface. These excited electrons migrate toward the surface and only escape if they possess sufficient energy to overcome the material's work function [5, 6]. Given the low accelerating voltage applied in this work (5 kV), only the secondary electrons representing the first few nanometers of the sample surface can exit and be detected [5, 6].

The construction of the micrographs is the result of signal amplification from the secondary electrons via the photomultiplier tube, which generates a two-dimensional intensity distribution represented as micrographs. This process yields a high-quality representation of the sample surface topography. The JEOLTMIT510 Scanning Electron Microscope was employed to generate the contiguous set of individual micrographs from which the full composite micrograph was assembled. The Image Montage capability within the JEOLInScopeTM

*Corresponding author.

Email address: katie.jones@plymouth.ac.uk (Katie L. Jones)

Could talk here about how we wanted to do resin impeg like Kane et al, but did not have the chance, and explain this might introduce issues, also we could talk about how this is quite rough, and that this kind of sample preparation (i.e. no vibratory polishing, no resin impregnation) is not ideal and may have introduced both artefacts and noise. Additionally, sonication may have

Table 1: Manufacturer dataset for IG-110 and IG-430 [3]

Grade	Coke source	Bulk density/g cm ⁻³	Filler particle size/ μm	Tensile strength/MPa	Young's modulus/GPa	Thermal conductivity/W m ⁻¹ K ⁻¹
IG-110	Petrol 1	1.77	10	25	9.8	120
IG-430	Pitch	1.82	10	37	10.8	140

package performed this function. The system captures multiple micrographs by using a motorized stage to move the electron beam over the specified area with a set overlap for each new micrograph. The software automatically adjusts stigmation, contrast, and brightness. Analysis of the metadata for all 1,350 micrographs demonstrated that shifts in contrast and brightness were minor, having a negligible impact therefore on the later selection of the intensity threshold for the full composite (Table 2) The complete set of selected parameters is tabulated in Table 3.

Table 2: Contrast (C) and Brightness (B) Summary by Sample

Variant	Avg C (%)	Std C (%)	Avg B (%)	Std B (%)
IG430B	98.01	1.02	99.69	0.08
IG430C	98.16	0.82	99.83	0.08
IG110B	95.86	0.72	99.26	0.13
IG110C	94.03	0.93	99.38	0.13
IG110F	98.20	0.70	99.69	0.13

In this work, a magnification of 1000X was selected as an optimal compromise between the resolution necessary for capturing the pore structure at the required scale and the total area covered by each micrograph. The scale of this study is significant, with each micrograph covering 12,288 μm^2 and each sample consisting of 225 micrographs, yielding a total imaging area of 2.765 mm² per sample. With 3 samples analysed per grade, the total scanned area per graphite grade is 8.294 mm². Given this scale, each composite micrograph represents a substantial section of the sample and captures a thousands of pores.

Huang
2021 used
5000×
magnification
with
48 micro-
graphs per
sample,
covering
0.13 mm
× 0.13 mm
for their
composite.

Table 3: Parameters for composite assembly captured with the JEOL IT510 SEM using Image Montage Mode

Parameters	Values
Magnification (×)	1000
Resolution ($\mu\text{m}/\text{px}$)	0.1
Surface area per micrograph (μm^2)	12 288
Overlap (%)	10
Micrographs per sample (n)	196

2.4. Composite assembly

The composite assembly stage ("stitching") , where the overlapping micrographs are combined into a single image per sample, may have a significant impact on the porosity values generated as incorrect fusion will misrepresent pore structures. To address this, a stitching method based on the phase correlation approach developed by Kuglin and Hines (1975) and further refined by Preibisch et al. (2009) was employed as an ImageJ plugin [7, 8].

One advantage of this method is the avoidance of error propagation by consecutive registration steps, as simply placing micrograph A relative to micrograph B, and then micrograph B relative to micrograph C, would result in accumulation of errors. This method builds a graph whose nodes are the micrographs, and edges are the measured pairwise shifts between the micrographs. It then finds the set of micrograph positions that minimize the total squared registration error across the entire graph, a form of globally optimized registration [8].

This stitching method also allows sub-pixel accuracy, which is crucial for accurate pore measurement. If each micrograph is a discrete 2D signal, then for any two micrographs A and B , which are shifted relative to each other (i.e., micrograph B is shifted two pixels up and 10 pixels left of micrograph A) then their Fourier transforms would have the same magnitude but different phases. A normalized cross-power spectrum isolates the phase difference, and from there the Inverse Fourier transform yields a correlation map with peaks indicating possible translations between the micrographs. Unfortunately, complexity of real images and the periodicity of the Fourier transform means that the correlation map is not a single peak, but rather a set of peaks, each representing a possible translation. This method therefore selects the n highest local maxima and finds the peak with the best correlation, which it defines as the true translation between the two micrographs [8]. Finally, sub-pixel accuracy in that shift is achieved by applying a parabolic interpolation around the selected peak to refine the translation estimate.

Additionally, a non-linear intensity blending

I actually
did 0-14 so
that is 15
x 15 which
is 225 mi-
crographs
per sam-
ple

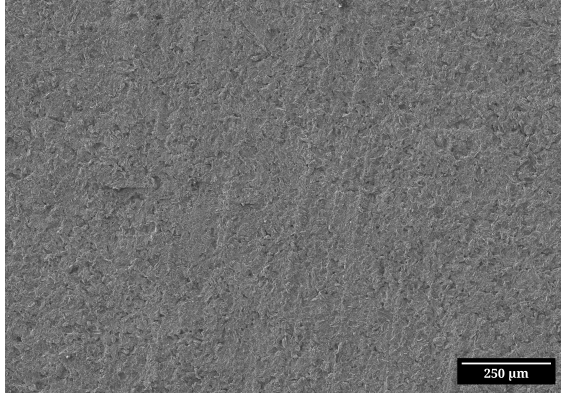


Figure 1: Fully assembled SEM composite: IG-430 Sample C, 1000 \times magnification, 5 kV accelerating voltage. Bar = 250 μm .

function eliminates the visible seams between micrographs, which can occur even when the micrographs are perfectly aligned due to shading variations. This blending assigns a weight to each pixel in a tile, working as a function of the distance from the tile edge, with the a tunable parameter controlling this weighting function. In non-overlapping regions, the centre of the micrograph, the weight is essentially 1, so the original pixel value is preserved exactly. In overlapping regions, intensities are a convex combination of the original values. Crucially, because the weights sum to 1 everywhere, blended intensity is simply a weighted average of the original intensities. Thus, the final composite micrograph is still a valid representation of the original micrographs, but the seams have been removed, and the transition between micrographs is smooth [?]. Testing indicated that different values in the blending parameter, which is tunable, had no discernable impact on the final composite micrograph, and therefore no impact on the final porosity values. By contrast, the removal of the visible seams between micrographs did increase confidence that in the following steps, the subsample used to determine the intensity threshold was representative of the full composite micrograph.

The resulting composite micrographs showed excellent alignment with no visible delineation between individual micrographs, a total area comparable with previous works, high resolution, and clear distinction between porosity and bulk when examined closely (Figure 1 [9, 10]).

2.5. Computation of Channel Porosity

2.5.1. Intensity/Greyscale Thresholding

For each 8-bit micrograph E (pixel values $0 \leq E(x, y) \leq 255$), we first compute its intensity histogram $H(i)$ for $i = 0, 1, \dots, 255$. Specifically,

$$H(i) = \sum_{x=1}^M \sum_{y=1}^N \mathbf{1}\{E(x, y) = i\},$$

where M and N are the image width and height (in pixels), and

$$\mathbf{1}\{E(x, y) = i\} = \begin{cases} 1, & \text{if the pixel at } (x, y) \text{ has intensity } i, \\ 0, & \text{otherwise.} \end{cases}$$

The indicator function $\mathbf{1}\{E(x, y) = i\}$ “tests” each pixel, yielding 1 if the pixel greyscale value equals i (e.g. greyscale value of 250), and 0 otherwise. The double sum $\sum_{x=1}^M \sum_{y=1}^N$ runs that test over every pixel in the micrograph resulting in a histogram $H(i)$ of 256 bins, each bin representing number of pixels in the micrograph at each greyscale value i .

Intensity thresholding then $H(i)$ determines a greyscale value at which porosity and bulk (i.e., foreground and background) are distinguished.

Global automatic thresholding algorithms optimise by different criteria (i.e. maximisation of inter-class variance, minimisation of intra-class variance) to determine thresholds. For manual selection of a given threshold, or validation of an automatically selected threshold, there exists no certain criteria to allow a fully objective evaluation [9]. Thresholding aims to select an intensity value that reliably binarizes porosity and bulk in a way that minimizes both Type I and II errors, as evaluated by the operator (i.e., false positives, classifying a pore where one is not present, and false negatives, not classifying a pore where one is present).

A test of all 17 of the available automatic thresholding methods available in ImageJ demonstrated that none of the available automatic global intensity thresholding algorithm effectively distinguished between porosity and bulk with the sensitivity required to allow the classification of pores for the given histogram (Figure 3). The key cause is likely the lack of a bimodal distribution in the histograms generated by any of the micrographs, meaning that there are statistically no classes to be separated (Figure 2).

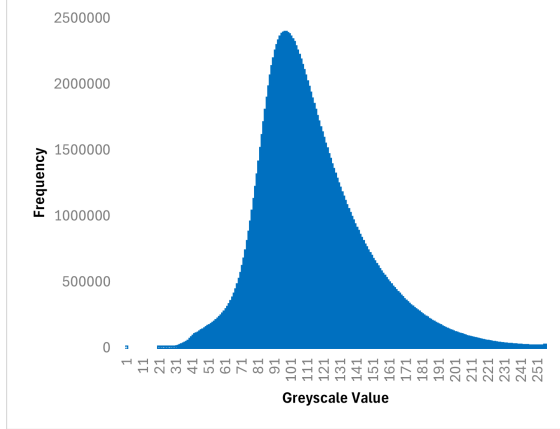


Figure 2: PLACEHOLDER DRAFT: Histogram of greyscale values for IG-430 Sample F, 1000 \times , Showing skewness and unimodality

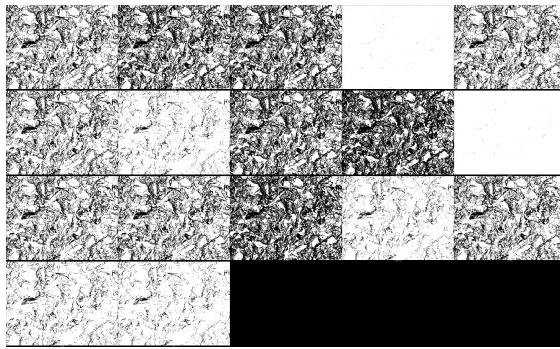


Figure 3: Thresholded Micrograph of IG-430 Sample C at 1000 \times Magnification. Methods are placed sequentially from right to left, row by row. (a) Default (b) Huang (c) Huang2 (d) Intermodes (e) IsoData (f) Li (g) MaxEntropy (h) Mean (i) MinError(I) (j) Minimum (k) Moments (l) Otsu (m) Percentile (n) RenyiEntropy (o) Shanbhag (p) Triangle (q) Yen

A HITL (human in the loop) approach was therefore undertaken, as illustrated in the process diagram (Figure 4). Here, the operator subsamples the composite micrograph, then examines this subsample to determine the threshold at which porosity and bulk are best separated. The operator then applies this threshold, along with a pore diameter threshold, to the full composite. The composite micrograph has therefore been binarized and porosity can be quantified via various connected component analysis algorithms, such as the "Analyse Particles" function in ImageJ.

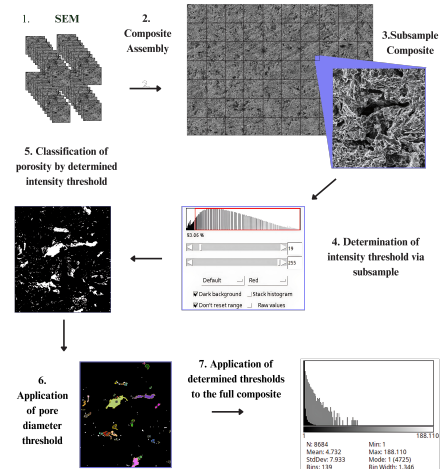


Figure 4: Full thresholding workflow detailing the process of micrograph generation, composite assembly, subsampling, intensity thresholding, and pore diameter thresholding.

An output from this process is exemplified, selected at random, which demonstrates excellent delineation of pores, according to an inevitably subjective operator evaluation (Figure 5).

2.5.2. Pore Diameter Thresholding

Pore size thresholds were imposed in this work, as in previous studies [11, 9, 10], to restrict the automated recognition of pores to a range (i.e., only counting pores $> 12.5\mu\text{m}^2$) where classification is deemed reliable. However, this approach is inherently limited by the practical difficulty of objectively determining whether any given pore classification is correct.

As shown in (Table 4), extreme changes in the total pore count result from minor alterations in the threshold, with a 0.5 μm^2 threshold yielding a

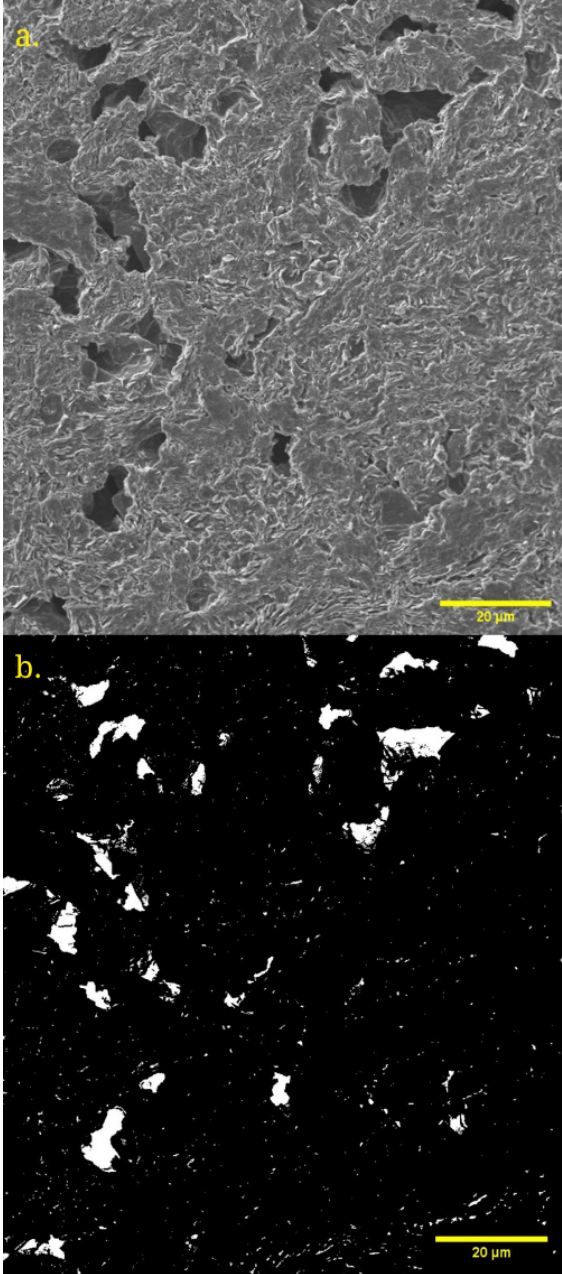


Figure 5: DRAFT: IG430F raw (a) and following intensiy thresholding (b)

Table 4: Effect of different pore area thresholds on a subsection of IG-430F, showing the resulting pore count, total area, average pore size, and percentage area.

Area Threshold (μm^2)	0	0.5	1	2	4	8
Count	254261	11375	6	4085	2812	1881
Total Area (μm^2)	71219	56722	53361	50063.63	46518	41161
Avg. Size (μm^2)	0.28	4.987	8.229	12.255	16.543	21.883
% Area	4.786	3.812	3.586	3.364	3.126	2.766

total pore count of 11,375, while a 1 μm^2 threshold yields a pore count of 6,485. Crucially however the total area of pores above the threshold remains relatively stable, with a porosity of 3.8% for the 0.5 μm^2 threshold, and 3.6% for the 1 μm^2 threshold. When combined with individual analyses of the resulting PSDs and precise examination of exactly which features are excluded at each threshold as per (Figure 6), a pore area threshold of 1 μm^2 (dia = 1.12 μm) was selected an optimal compromise between type I and II errors.

Crucially, setting such a threshold does not imply that no pores exist below this limit. Rather, it acknowledges that the confidence in classifying pores below the threshold is too low for reliable use. In this work, the limitations of any single technique are compensated by the strengths of others. during modelling, an interval is selected over which the channel porosity determined from SEM imaging can reliably constrain the outputs of the inverse modelling process. Thus, no type II errors are introduced in the final model due to pore size thresholding, thanks to the combined use of alternative techniques and the ability to specify an interval within PoreXpert v.3.

2.5.3. Channel Porosity Analysis and Calculation

Following the determination of the above thresholds, the channel porosity was calculated using the “Analyse Particles” function in ImageJ. This function scans the micrograph pixel by pixel, identifies all pixels that surpass the intensity threshold, and groups them into connected regions via a flood-fill algorithm. Connectivity is defined based on the 8-connected (Moore neighborhood) criterion, whereby a pixel at (x, y) is considered connected to its eight immediate neighbors:

$$(x - 1, y - 1), (x - 1, y), (x - 1, y + 1), (x, y - 1), \\ (x, y + 1), (x + 1, y - 1), (x + 1, y), (x + 1, y + 1)$$

Thus, any two pixels that exceed the intensity threshold and are either directly adjacent or diag-

This part really requires Peter's insight as to the actual functioning of the program

This is not the key issue. The real thing is the accuracy of the pore size distribution generated by SEM. For example, the modelling would I think be distorted completely by saying that 3% of

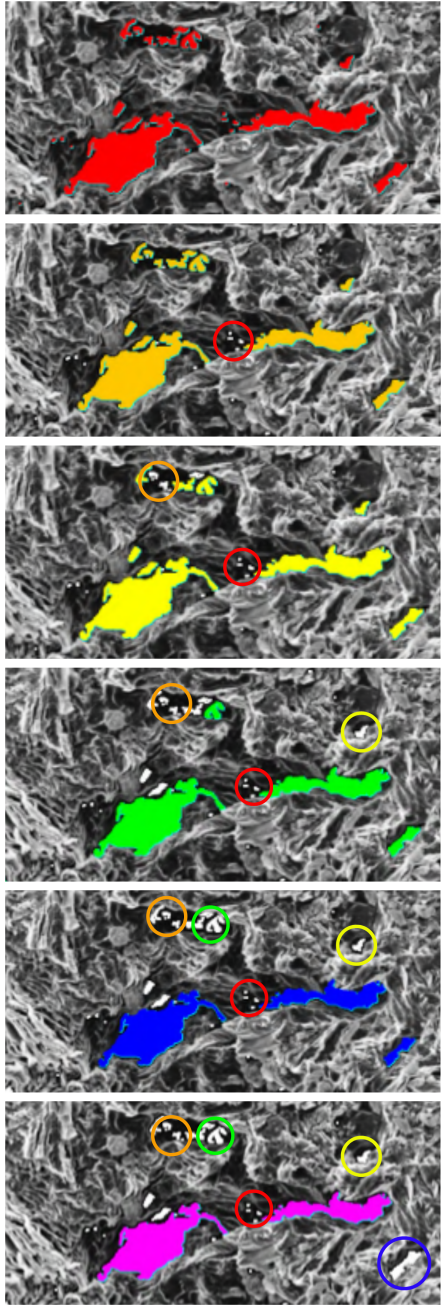


Figure 6: Effect of minimum area threshold on pore identification in subsample of IG-110 Sample B. Highlighted circles denote features which surpassed the previous threshold(s) only, indicated by colour. Thresholds applied (a-f, left-to-right, top-to-bottom): None, $0.5 \mu\text{m}^2$, $1 \mu\text{m}^2$, $2 \mu\text{m}^2$, $4 \mu\text{m}^2$, and $8 \mu\text{m}^2$.

onally connected are classified as belonging to the same region (pore). The function then computes the area of each pore by converting the pixel count into physical area (i.e., 10 pixels per micrometre). Regions that do not meet the area threshold are omitted. The final results are a pore size distribution (PSD) and the channel porosity (%).

For the same subsample of IG430F as above, the result of intensity thresholding followed by pore diameter thresholding at $1.12 \mu\text{m}$ diameter is exemplified, demonstrating a high degree of accuracy as evaluated by the operator, especially given the particular focus at this stage in excluding Type I rather Type II errors (Figure 7)

2.6. Helium (He) Pycnometry

Skeletal density was obtained using a Pycnometric ATC pycnometer (Thermo Fisher Scientific, Italy) at a temperature of $20.00 \pm 0.01^\circ\text{C}$. Measurements were taken in ten replicates per sample, calculating the arithmetic mean.

Solid phase volume V_{SOLID} was calculated assuming a theoretical density of g cm^{-3} for an ideal graphite crystal. Closed Pore Volume (CPV) and Open Pore Volume (OPV) for each of the samples was calculated via equations 1 and 2.

$$\text{CPV} = \frac{m - V_{\text{SOLID}} \times \rho_s}{\rho_s} \quad (1)$$

$$\text{OPV} = V_{\text{BULK}} - \text{CPV} - V_{\text{SOLID}} \quad (2)$$

Specific Pore Volume (SPV), the void volume accessible to helium per gram of sample was calculated via Equation 3.

$$\text{SPV} = \frac{1}{\rho_s} - \frac{1}{\rho} \quad (3)$$

2.7. Mercury (Hg) Intrusion Porosimetry

Mercury intrusion porosimetry operates on the fundamental principle that the pressure at which a non-wetting fluid intrudes a given pore is inversely proportional to the diameter of that pore (i.e., the larger the pore, the easier it is for the non-wetting fluid to enter it). The exact physical relationship between diameter and applied pressure is governed by the Laplace Equation (Eq. 4)

$$d = \frac{-4\gamma \cos \theta}{P} \quad (4)$$

The pore diameter d is calculated using the equation:

insert theoretical density here

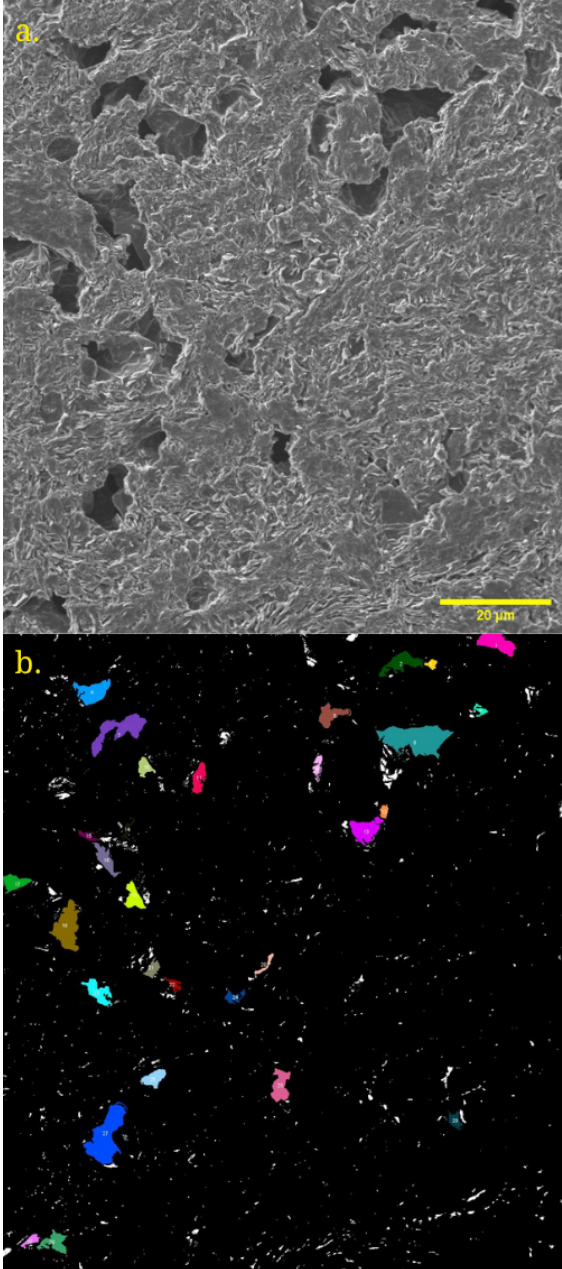


Figure 7: Draft: IG-43F subsample a. Raw and b. After intensity and pore diameter thresholding

- d (m): Pore diameter
- γ (N/m): Surface tension of the fluid
- θ (degrees): Contact angle of the fluid with the surface
- P_{app} (P): Pressure

Values of 140° and 130° were used for advancing and receding contact angles respectively, while a value of 0.480 N m^{-1} was assumed for the surface tension of mercury [12].

In this work, the dataset generated by Jones et al. [3] was used, representing measurements performed not only on the same grades of graphite, but the same batch of graphites (i.e. sampled from the same larger "brick") as those samples which underwent SEM imaging and He pycnometry in this work.

2.8. Nitrogen (N_2) Adsorption

Low-pressure gas adsorption isotherms were obtained using a BELSORP-max volumetric gas adsorption instrument (MicrotracBEL, Japan).

As with mercury intrusion porosimetry, the dataset generated by Jones et al. [3] was used in this work. Once more, this represents measurements performed on the same grades but the same batch of graphites (i.e. sampled from the same larger "brick") as those samples which underwent SEM imaging and He pycnometry in this work.

3. Modelling

PoreXpert is a void network simulation package developed at the University of Plymouth, and now marketed worldwide by the University's spin-out company, PoreXpert Ltd. A primary input for its modelling is the percolation characteristic of the sample, usually measured by Hg porosimetry. In the case of nuclear graphite, mercury porosimeters cannot reach sufficient applied pressure to probe the smallest voids of interest, and therefore, the percolation characteristic is extended to smaller void sizes by Grand-Canonical Monte-Carlo interpretation of N_2 adsorption. PoreXpert is a quasi-Bayesian model which proceeds inversely from effect (the percolation) to cause (the void network). PoreXpert constructs an 8 dimensional parameter space, composed of 5 numerical parameters which represent the physical characteristics of the pore network, such as the skew of the void (pore) size

distribution, and 3 constraining Boolean parameters, for example, to avoid structures where features overlap each other. A Boltzmann-annealed amoeboid simplex searches over this parameter space to find the set of parameters that produces a percolation curve minimally different from the intrusion curve derived from Hg porosimetry and N₂/Kr adsorption. The final result is a simulated pore network with the correct porosity and percolation properties, on which many simulations, such as pore-fluid permeability and tortuosity, and sample ageing under radiation, can be performed [13].

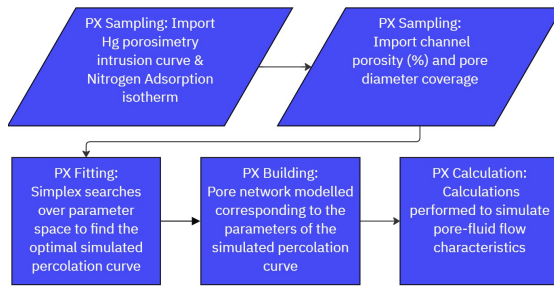


Figure 8: Full modelling pipeline, within the PoreXpert software package, integrating intrusion and SEM-derived datasets

Modelling, conducted in PoreXpert v.3, was processed according to the illustrated workflow (Figure 8). The user selects the approximation types that best reflects their interpretation of the depth of imaging into the porous structure (Figure 9, [13]), Approximation Type 1 *Surface connected throats only* is likely to be a more accurate approximation for the channel porosity dataset constructed in this work, as a consequence of the stringent intensity threshold applied. However, due to stability challenges in this early compilation, approximation Type 2 *Surface connected throats and the visible volumes of connected pores* was applied instead (Figure 9).

Following the selection of parameters, the channel porosity data were entered into the PoreXpert v.3 interface including a minimum and maximum pore diameter as per (Figure 4), the model was able to adjust the extent of the PSD which the channel porosity estimates, optimising effectively to a minimal distance distance of 1.91% deviation from the experimental curve (Figure 10)

The result is a pore network, upon which many simulations can be performed. 11 shows a 3D rendering of the pore network generated by PoreXpert.

Without being able to run it, you could not verify, so I think it would be better to just specify the approximation type.

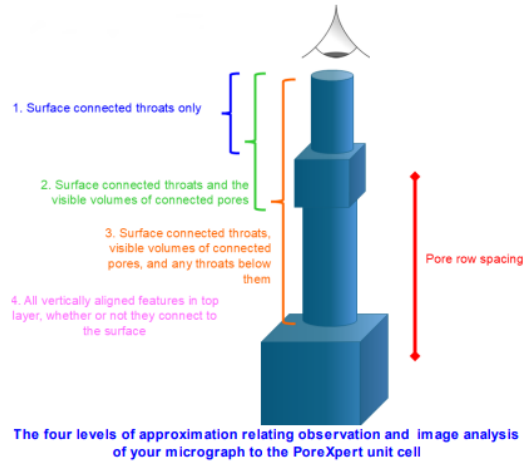


Figure 9: DRAFT: Does it belong? //Approximation types available for user selection in PoreXpert v.3, selected by the user through validation based on the thresholds applied and the extent of the insight into the given media

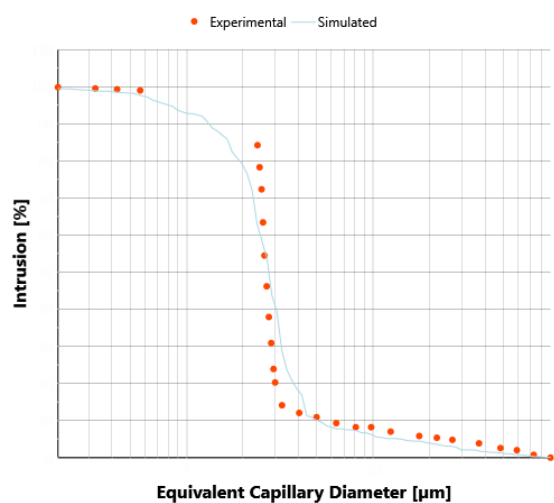


Figure 10: PX Fitting process as per (Figure 8). Orange dots denote experimental datapoints, the blue line is the simulated percolation curve resulting from a pore network of physically plausible parameters.

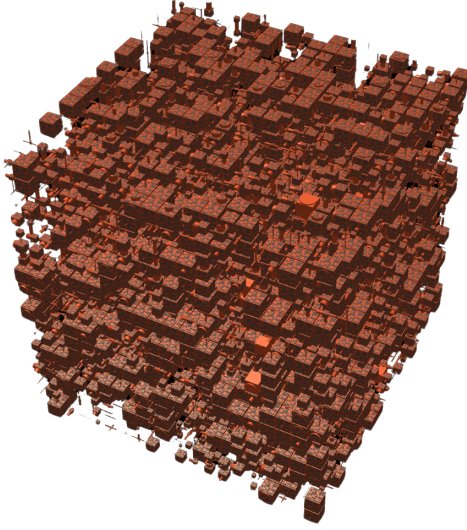


Figure 11: PoreXpert visualisation of the pore network resulting from the integration of channel porosity and experimental data by the workflows above. 1.91% distance between simulated and experimental curves, following the application of Approximation Type 2 (Figure 9). Channel Porosity estimation was averaged over the top 9 layers of a unit cell 20x20x20. The result of one generation of stochastic number generation. Run in Direct Mode as Batch mode remained unstable in this early compilation

Table 5: Pore Size Distribution (PSD) and summary characteristics for IG-110 and IG-430 samples, tabulating number of pores, total pore area, and channel porosity.

Sample	n / pores	Total Area / μm^2	Channel Porosity / %
IG110 B	8,684	41,091	3.14
IG110 C	7,075	49,755	3.27
IG110 F	8,296	50,735	3.38
IG430 B	6,848	32,983	2.30
IG430 C	13,026	49,534	2.94
IG430 F	6,819	56,794	3.66

Initial testing of PoreXpert modelling demonstrate excellent congruence with manufacturer datasets, as exemplified below on IG-110 Sample B. Crucially, the linear trend line shows only a weak correlation between open porosity estimate and distance between simulated and experimental percolation characteristic ($r^2 = 0.32$) (Figure 12). Thus, taking the average over all stochastic generations of PoreXpert is a valid measure of this method's estimate of open porosity.

Initial modelling generated plausible data...

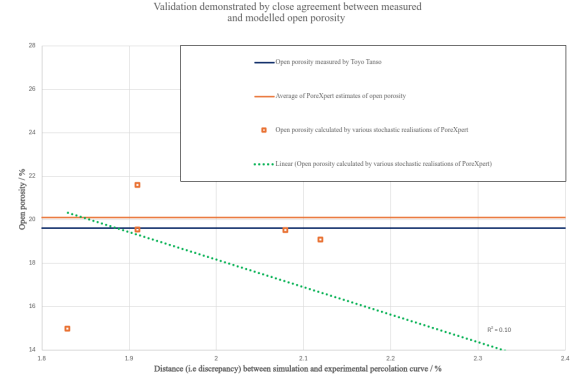


Figure 12: DRAFT: Needs to be reformatted for publication, if we choose to keep it. Validation of modelled open porosity by comparison of modelled open porosities generated by PoreXpert with manufacturer data for IG-110, which estimates a 19.62% open porosity [3]

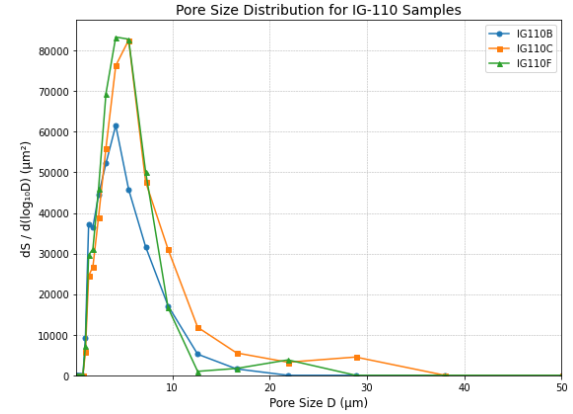


Figure 13: DRAFT: I want to recheck my code on these distributions

4. Results

The completed workflow of SEM imaging and computational composite analysis yielded estimates of channel porosity for both graphite grades (Table 5). IG-110 samples exhibited channel porosity values ranging from 3.14-3.38%, while IG-430 samples showed greater variability, ranging from 2.30-3.66%

Area contribution distribution is represented graphically for both graphite grades (Figure 13, 14). The area of each logarithmic bin (spanning 0.1-100 μm on the x-axis) was summed then divided by the bin width in $\log_{10}(D)$ to derive $dS/d(\log_{10} D)$, with the x-axis then linearised. y-axis values represent area density in μm^2 per $\log_{10}(D)$.

IG-110 and IG-430 both exhibit a peak in the sub-10 μm range. This is the inverse of trends ob-

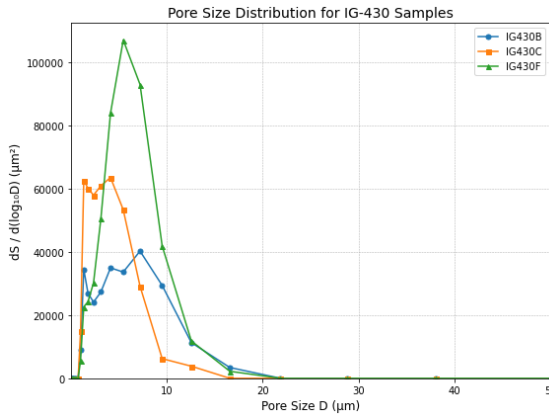


Figure 14: DRAFT: I want to recheck my code on these distributions

served in previous OM-based analyses, where the majority of the porosity is contributed by pores above this range [9]. [14] found that porosity as by classified SEM, albeit with a different distribution, was 3% for IG-110, which is highly congruent with the 3.14–3.38% range derived in this work.

Interpolation increases confidence in the basic functionality of this method. Adjustment of the intensity threshold to match previous OM works (i.e., pore contours and pore throats are no longer distinguished, via a reduction in intensity threshold) produces highly similar channel porosity values. Specifically, [10] estimated a channel porosity of 14.73% for IG-110, with [9] deriving 14% for the same grade, highly congruent with the approximately 13–14% figure this method derives with an adjusted intensity threshold, but also illustrating the scale of the impact in intensity threshold selection on the final channel porosity estimate.

5. Discussion

5.1. Channel Porosity Overestimation due to connectivity algo

This algorithm is likely to yield at least a slight overestimation of the channel porosity. This is because such an inclusive definition means that two or more pores, connected by a narrow neck or even simply with adjacent pixels, would be classified as a single pore. Notably, this would not change the final channel porosity (%), at least in isolation, but would result in a rightward shift in the PSD. Skeleton segmentation is for fine-grade nuclear graphite likely to be a more accurate approach than a simple

connectivity algorithm as used here would be a key improvement if implemented [15]

5.2. Pore Fragmentation and Implications for Modelling

The application of a maximum pore diameter is a key part of the modelling as initial modelling where this was not implemented failed to yield reliable results. It is believed that this is due to the impossibility of the model fitting an plausible network on the premise that pores from 1.12 μm diameter upwards represent only 3 % of the sample surface. Imposing an upper threshold as the simple max of the pore diameters identified by SEM is an uncomplicated initial solution which has more logical implications (i.e., to state that between 1.12 and 20 μm diameter, 3% of the sample surface is represented by porosity). This threshold varied between 13–26 μm in this work, which should cover the vast majority of the porosity, particularly given the pore fragmentation issue described below.

Specifically, the use of a simple Moore neighbourhood connectivity, when combined with the fact that Erosion and Dilatation binary operations were not applied, means that pores which the operator identifies as a single pore are in more than one case instead defined as two or more pores. Not only this but these split pores may not then surpass the pore diameter threshold of 1.12 μm . (e.g., a pore of 10 μm diameter might be split into 2 pores, 1 of 9 μm diameter and another of 1 μm diameter, which would be discarded due to the pore diameter threshold, reducing the channel porosity % and shifting rightward the pore size distribution).

The end result is that it is difficult to describe the pore size distribution derived from SEM as it currently stands, as completely impenetrable. Crucially, the production of reasonable results from the modelling as above depends on an accurate constraint of the pore diameter interval (i.e., the channel porosity figure of 3% refers only to porosity between 1.12 and 25 μm diameter) and so not only the SEM-derived pore size distribution but the PX modelling which uses it, has at least some reduction in reliability due to the pore fragmentation issue. However, this is likely a soluble problem, as follows.

5.3. Proposed Future Workflow

-Just my idea of an improved workflow: 1. Resin Impregnation 2. SEM (see if we can go to 2kV)

3. Otsu Thresholding (We have clear bimodality thanks to Resin impregnation) 4. Skeleton segmentation (Avizo software needed?) 5. Apply improved pore diameter thresholds, or maybe do not do any at all as no longer needed? At least lowered. 6. Modelling

References

- [1] Toyo Tanso Co., Ltd., Atomic power and nuclear fusion, accessed April 21, 2025 (2025). URL <https://www.toyotanso.com/us/en/Products/applications/porosityandporeshape.html>
- [2] ASTM International, D7219-19 Standard Specification for Isotropic and Near-isotropic Nuclear Graphites, published August 2019; supersedes D7219-08R14 (2019).
- [3] K. Jones, G. Laudone, G. Matthews, A multi-technique experimental and modelling study of the porous structure of ig-110 and ig-430 nuclear graphite, *Carbon* 128 (2018) 1–11. doi:10.1016/j.carbon.2017.11.076.
- [4] N. Fang, R. Birch, T. Britton, Optimizing broad ion beam polishing of zircaloy-4 for electron backscatter diffraction analysis, *Micron* 159 (2022) 103268. doi:10.1016/j.micron.2022.103268.
- [5] O.-W. Achaw, A study of the porosity of activated carbons using the scanning electron microscope, in: V. Kazmiruk (Ed.), *Scanning Electron Microscopy*, IntechOpen, Rijeka, 2012, Ch. 24. doi:10.5772/36337. URL <https://doi.org/10.5772/36337>
- [6] J. I. Goldstein, D. E. Newbury, P. Echlin, D. C. Joy, C. E. Lyman, E. Lifshin, L. Sawyer, J. R. Michael, *Scanning Electron Microscopy and X-Ray Microanalysis*, 3rd Edition, Springer Science+Business Media, New York, 2003. doi:10.1007/978-1-4615-0215-9. URL <http://extras.springer.com>
- [7] C. Kuglin, D. Hines, The phase correlation image alignment method, in: *Proceedings of the International Conference on Cybernetics and Society*, 1975, pp. 163–165.
- [8] S. Preibisch, S. Saalfeld, P. Tomancak, Globally optimal stitching of tiled 3d microscopic image acquisitions, *Bioinformatics* 25 (11) (2009) 1463–1465. arXiv:2009 Apr 3, doi:10.1093/bioinformatics/btp184.
- [9] Q. Huang, H. Tang, Porosity analysis of superfine-grain graphite ig-110 and ultrafine-grain graphite t220, *Materials Science and Technology* 35 (8) (2019) 962–968. doi:10.1080/02670836.2019.1599557.
- [10] J. Kane, et al., Microstructural characterization and pore structure analysis of nuclear graphite, *Journal of Nuclear Materials* 415 (2) (2011) 189–197. URL <https://www.toyotanso.com/us/en/Products/applications/porosityandporeshape.html>
- [11] J. Taylor, G. Hall, P. Mummery, Investigating the effects of stress on the pore structures of nuclear grade graphites, *Journal of Nuclear Materials* 470 (2016) 216–228. doi:10.1016/j.jnucmat.2015.12.031.
- [12] J. Van Brakel, S. Modrý, M. Svatá, Mercury porosimetry: state of the art, *Powder Technology* 29 (1) (1981) 1–12. doi:[https://doi.org/10.1016/0032-5910\(81\)85001-2](https://doi.org/10.1016/0032-5910(81)85001-2). URL <https://www.sciencedirect.com/science/article/pii/0032591081850012>
- [13] G. P. Matthews, *PoreXpert User Manual: A comprehensive guide to version 3*, PoreXpert Ltd, Plymouth, UK, 3rd Edition, director and CEO, PoreXpert Ltd; Emeritus Professor of Applied Physical Chemistry, University of Plymouth, UK. Includes introductory tutorials, fundamental science sections, guidance on avoiding common experimental errors, and software validation. (2025). URL <https://www.porexpert.com/>
- [14] Q. Huang, H. Tang, A statistical analysis of pores and microcracks in nuclear graphite, *Shanghai Institute of Applied Physics, Chinese Academy of SciencesCorrespondence to Qing Huang, Email: huangqing2012@sinap.ac.cn* (2021).
- [15] J. D. Arregui-Mena, R. N. Worth, W. Bodel, B. März, W. Li, A. A. Campbell, E. Cakmak, N. Gallego, C. Contescu, P. D. Edmondson, Multiscale characterization and comparison of historical and modern nuclear graphite grades, *Materials Characterization* 190 (2022) 112047. doi:<https://doi.org/10.1016/j.matchar.2022.112047>. URL <https://www.sciencedirect.com/science/article/pii/S0025624X22000375>